nature energy

Supplementary information

https://doi.org/10.1038/s41560-026-02118-2

Diffusion-like overpotentials from non-diffusion mechanisms in battery particles

In the format provided by the authors and unedited

Supplementary Information

Supplementary Notes

Supplementary Note 1 Agglomerate particle morphology, size distribution, and porosity

The cathode active material used in this study are agglomerate particles of $Li_xNi_{1/3}Mn_{1/3}Co_{1/3}O_2$ composition, produced by Toda. The morphology as observed with scanning electron microscopy (SEM) is shown in Supplementary Fig. 1.

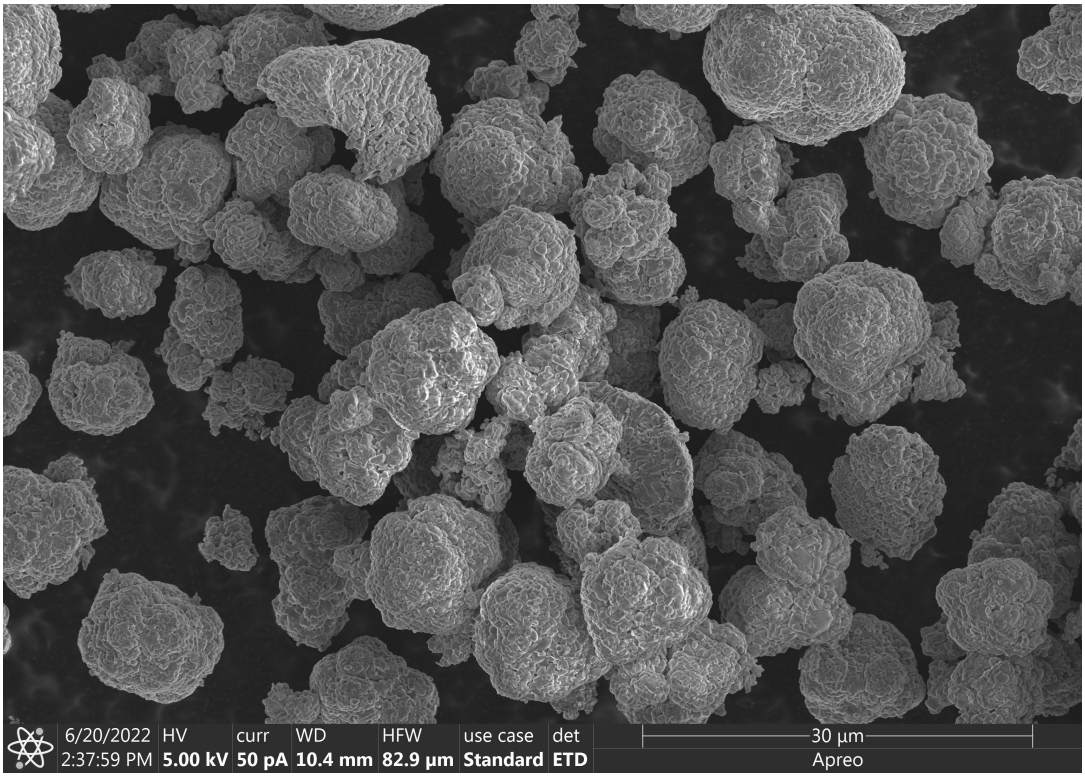

Supplementary Fig. 1: SEM image of polycrystalline NMC111 material (Toda) used in this study

Based on Particle Size Analysis (PSA) measurements, the most probable agglomerate particle size is about 11 µm in diameter (Supplementary Fig. 2). Using a hard-sphere model (assuming 100 % dense spheres), the PSA measurement can be converted to a mass-specific surface area of $0.120\,m^2\,g^{-1}$ for this material. This hard-sphere model essentially assumes no surface roughness or penetrable porosity within the agglomerate particles. By contrast, the estimated surface area from BET measurements for the same material using N_2 gas is $0.565\,m^2\,g^{-1}$ (for this analysis, we used the "BET surface identification" package[S1]). The difference between the two measured surface areas suggests a large amount of porosity (probed as estimated surface area) exists even in the undelithiated agglomerate particles.

The particle porosity measured with nano-computed tomography (nano-CT) was about 0.5 % at an undelithiated state (Supplementary Fig. 3). We note that this porosity value only captures

pores of sizes above the resolution limit of the technique, which is around 50 nm. While most of the pores as observed in nano-CT are closed pores (Supplementary Fig. 3b-c), BET and He pycnometry measurements, which use gaseous species capable of penetrating into much smaller pores, indicate that the majority of these pores are open pores. BET measurements show surface area that is 4.7 times the hard-sphere equivalent, and He pycnometry yields 100 % of the crystallographically calculated density. These measurements imply the existence of a porous structure below the 50 nm resolution limit.

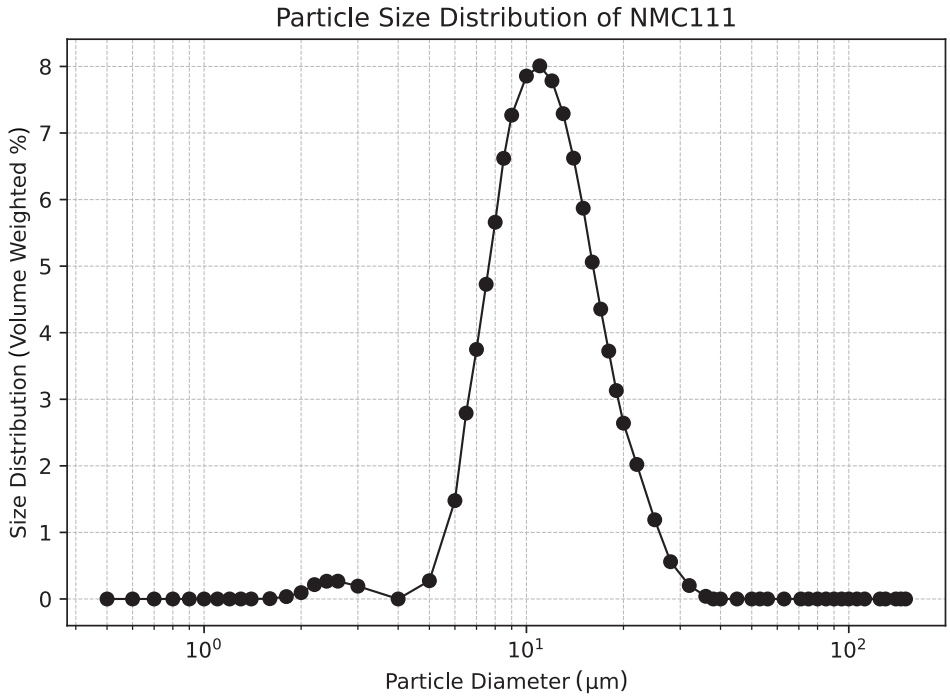

Supplementary Fig. 2: PSA results of polycrystalline NMC111 material (Toda) used in this study. The volume-weighted size distribution is shown.

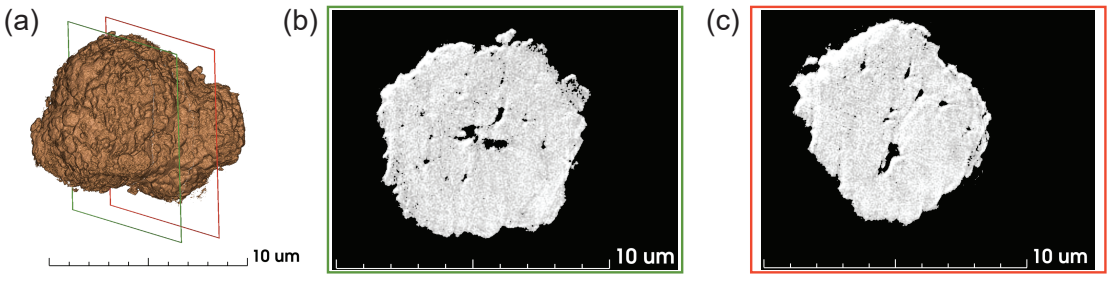

Supplementary Fig. 3: A nano-computed tomography image of a representative NMC111 agglomerate particle **(a)** 3D reconstruction of a NMC111 agglomerate particle. **(b)** A cross section image corresponding to the green frame in (a). **(c)** A cross section image corresponding to the red frame in (a).

Supplementary Note 2 Preparing 3-electrode coin cells

For electrochemical impedance spectroscopy (EIS) measurements, it is important for the reference electrode to be placed inside the electrode stack. For all electrochemical measurements, we therefore use a 3-electrode coin cell configuration as reported in Kuo *et al.* (Supplementary Fig. 4).[S2] The reference electrode Li chemical potential is established by electroplating Li onto the Cu mesh inserted inside the stack. An example electrochemical profile is shown in Supplementary Fig. 5.

Successful isolation of the working electrode can be confirmed by comparing the EIS spectrum of the working electrode in a 2-electrode and 3-electrode configuration. Shown in in Supplementary Fig. 6 is a Nyquist plot of a NMC111 working electrode impedance of a given cell when measured against the counter electrode (2-electrode configuration) and reference electrode (3-electrode configuration). The spectra show a significant difference, where one of the semicircle arcs is absent in the 3-electrode configuration. This absence indicates that the semicircle dominated by the negative electrode is excluded by the reference electrode configuration.

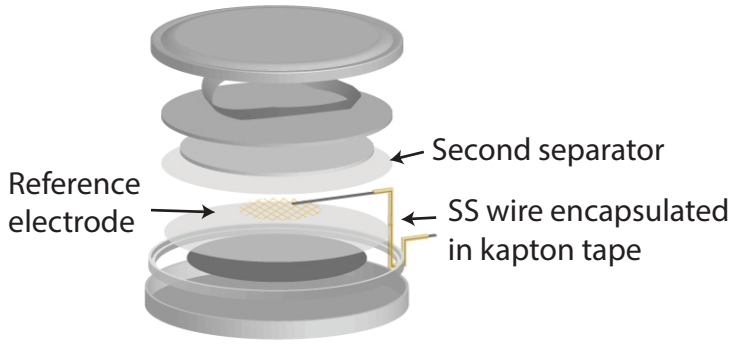

Supplementary Fig. 4: 3-electrode coin cell design from Kuo *et al.*[S2] A walkthrough video of the assembly process can be found online at: https://www.youtube.com/watch?v=KmtzLLjJ74A.

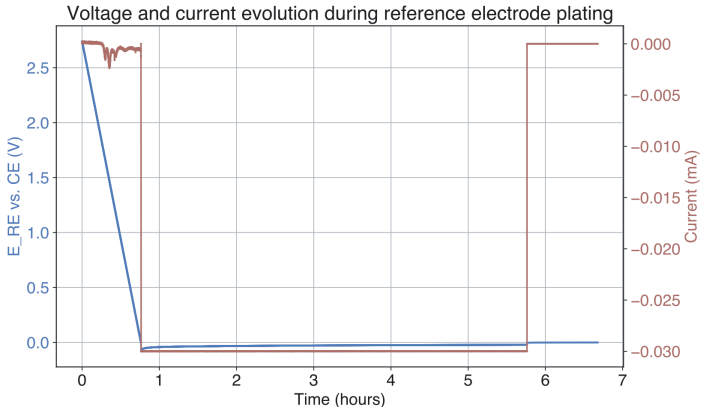

Supplementary Fig. 5: Example voltage and current curves during reference electrode plating.

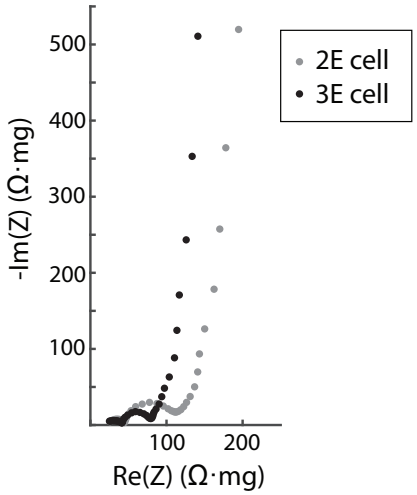

Supplementary Fig. 6: Nyquist plot of EIS measurements from a 2-electrode (2E) vs. 3-electrode (3E) coin cell (half-cell of NMC111 vs. Li)

Supplementary Note 3 Electrolyte densities and molarity corrections

The electrolytes molar concentrations quoted in the manuscript should be corrected based on measured deviations in density. Supplementary Tables 1 and 2 show our density measurements and the corresponding corrections. Density numbers are reported to the digit where we did not see deviations upon repeated measurements for a given electrolyte sample.

Measured Electrolyte Density (g/mL)	1.228	1.155	1.145	1.135	1.132
Reported Electrolyte Concentration (M)	1.0	0.4	0.2	0.1	0.05
Actual Electrolyte Concentration (M)	1.0	0.378	0.187	0.093	0.047

Supplementary Table 1: Electrolyte densities and actual molar concentrations for $LiPF_6$ salt in EC/DEC.

Measured Electrolyte Density (g/mL)	1.185	1.138	1.131	1.126	1.127
Reported Electrolyte Concentration (M)	1.0	0.4	0.2	0.1	0.05
Actual Electrolyte Concentration (M)	1.0	0.412	0.194	0.097	0.050

Supplementary Table 2: Electrolyte densities and actual molar concentrations for $LiClO_4$ salt in EC/DEC.

Supplementary Note 4 EIS analysis with different equivalent circuits

Since the EIS measurements are phenomenologically parameterized, a number of different equivalent circuits could be used for the analysis. An example of fitting the experimental EIS measurements with the equivalent circuit noted in the main text (Fig.2) is shown below (Supplementary Fig. 7).

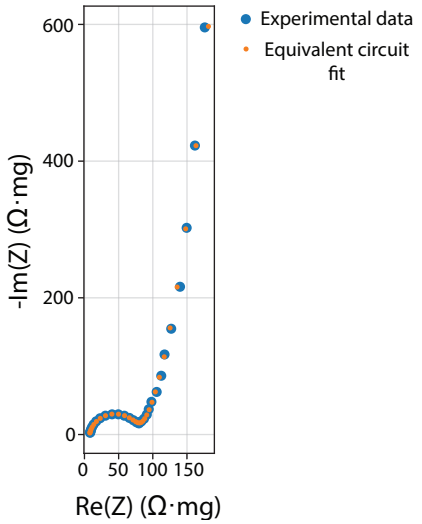

Supplementary Fig. 7: Example EIS fitting with an equivalent circuit.

To confirm that researchers would have analyzed similar correlations between R_{CT} and A_w from the measured EIS spectra, we have considered other equivalent circuits commonly used in the literature.

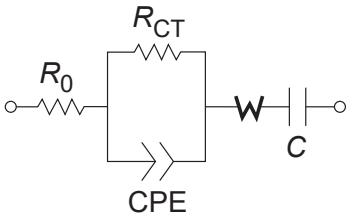

Supplementary Fig. 8: An alternative equivalent circuit that puts a Warburg component in series with both the R_{CT} and CPE components, unlike the Randles circuit.

First, we use an equivalent circuit with a semi-infinite Warburg component in series with R_{CT}//CPE. This circuit, shown in Supplementary Fig. 8, was chosen for its ability to fit the main features of the measured spectra, while simultaneously minimizing the number of parameters. Adding a capacitor in series to the rest of the circuit captures bounded diffusive and non-planar

geometrical effects using one parameter. Note that the circuit is not intended to represent every single physical process occurring in the system accurately. The results in Supplementary Fig. 9 show trends similar to those presented in the main text.

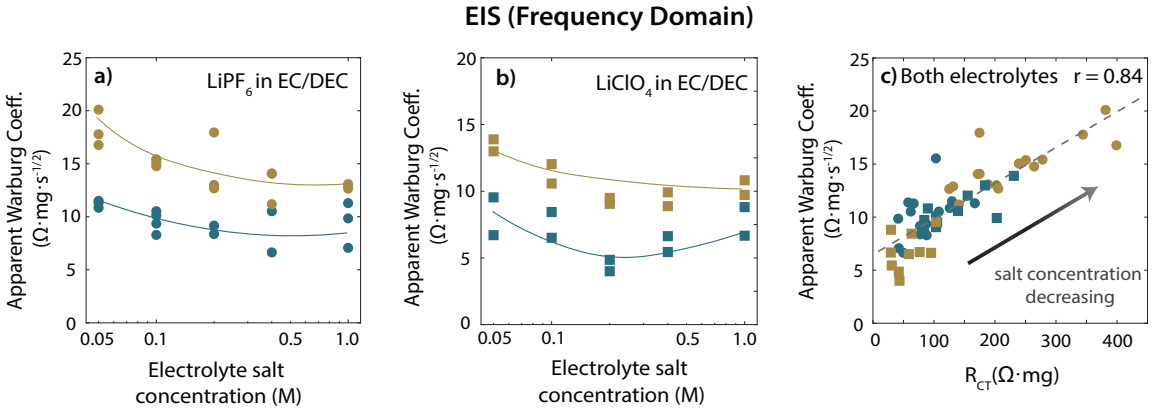

Supplementary Fig. 9: EIS measurements presented in the Fig. 3 re-analyzed using the alternative equivalent circuit in Fig. 8. **(a)** Extracted Warburg coefficients from EIS measurements vs. $LiPF_6$ salt concentration in the electrolyte. **(b)** Extracted Warburg coefficient from EIS measurements vs. $LiClO_4$ salt concentration. **(c)** Apparent Warburg coefficients extracted for both electrolytes vs. R_{CT}, with both values extracted from EIS measurements.

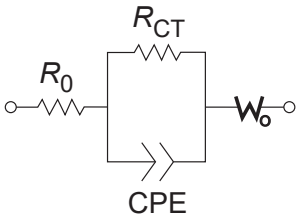

Supplementary Fig. 10: Another alternative equivalent circuit that uses a Warburg component with a finite length in place of a series of a semi-infinite Warburg and a capacitor. The Warburg component used here is an "open" type.

Next, we consider the case where finite-length effects are captured directly with the Warburg component, rather than through a series capacitor. This approach uses an "open" (or "reflective") type Warburg component, defined as:

$$Z_{\mathrm{W_O}} = \frac{Z_0}{\sqrt{j\omega\tau}} \coth(\sqrt{j\omega\tau}), \tag{S1}$$

as shown in Supplementary Fig. 10. Z_0 scales the impedance magnitude and τ captures the characteristic diffusion time. In this case, diffusion kinetics is captured primarily with the time scale parameter τ rather than with the impedance vs. frequency scaling behavior. As a result, the τ

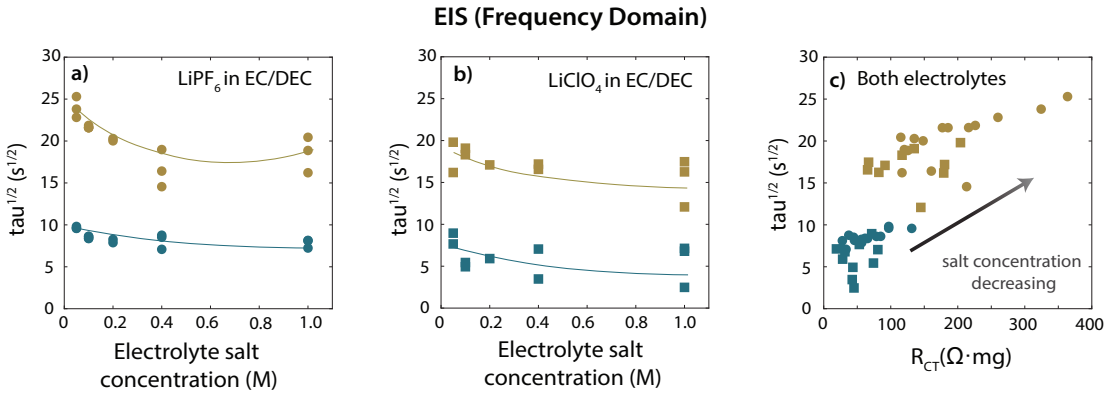

Supplementary Fig. 11: EIS measurements presented in Fig. 3 re-analyzed using the alternative equivalent circuit in Fig. 10. **(a)** Extracted $\sqrt{\tau}$ parameter vs. $LiPF_6$ salt concentration in the electrolyte. **(b)** Extracted $\sqrt{\tau}$ parameter vs. $LiClO_4$ salt concentration. **(c)** Extracted $\sqrt{\tau}$ parameter for both electrolytes vs. R_{CT}.

parameter extracted from this analysis method cannot be compared directly with the Warburg coefficient captured using a semi-infinite Warburg component.

Nevertheless, from analyzing EIS data with the equivalent circuit in Supplementary Fig. 10, we find results similar to the outcome of analyzing the Warburg coefficient of a semi-infinite Warburg component. As shown in Supplementary Figs. 11a-b, $\sqrt{\tau}$ depends on the electrolyte composition. Furthermore, we observe a positive correlation between $\sqrt{\tau}$ and R_{CT}. Overall, this alternative analysis method also supports the argument that the low frequency impedance is not solely governed by solid-state diffusion.

Supplementary Note 5 Apparent Warburg coefficient extraction from GITT measurements

For time-domain extraction of apparent Warburg coefficients, we analyzed the relaxation curve of GITT experiments using a modified time variable: $\sqrt{t_{relax}+\tau}-\sqrt{t_{relax}}$, where τ is the pulse duration and t_{relax} is the time elapsed since the termination of the current pulse.[S3,S4] Shown in Supplementary Fig. 12a is the model behavior corresponding to an isolated diffusion-controlled process (semi-infinite length diffusion). Supplementary Figs. 12b-c are some example fitting cases.

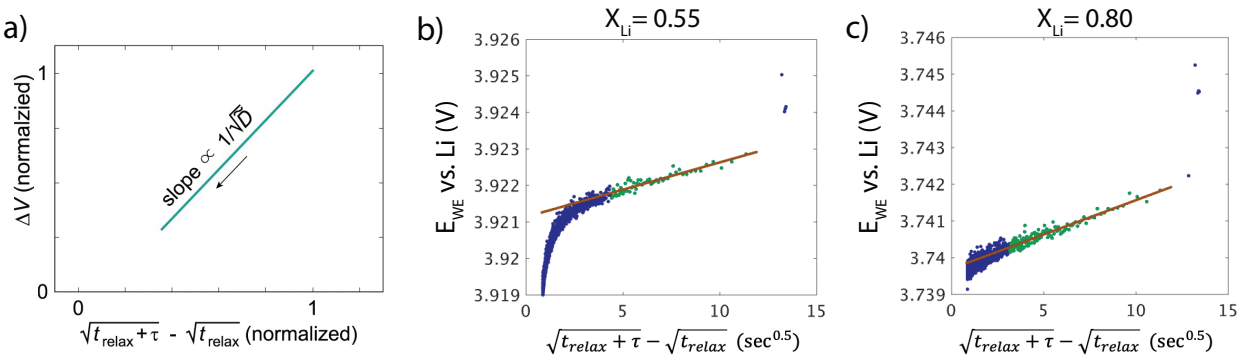

Supplementary Fig. 12: GITT analysis demonstration. **(a)** Relaxation behavior of a purely diffusion-controlled system with a semi-infinite geometry, showing a linear relaxation curve with respect to a modified time variable devised for the analysis, from [S3]. **(b)** Example fitting case from a pulse-relaxation trial data measured at 3.93 V vs. Li (Li fraction 0.55). **(c)** Example fitting case from a pulse-relaxation trial data measured at 3.74 V vs. Li (Li fraction 0.80). The highlighted data in green were used for linear fitting. Six such pulse-relaxation experiments are combined to extract A_w at a given condition.

Supplementary Note 6 Porous and dense particle models

The aim of this model is to evaluate the impact of electrolyte penetration into the pores of agglomerate particles, while intentionally excluding both solid state diffusion effects and electrolyte salt diffusion effects. For this purpose, we construct a porous particle model, where the penetrated electrolyte makes parts of the particle interior available for electrochemical reactions (i.e. the electrochemically active area is not only at the particle outer boundary, but also within the porous interior).

Governing Equations

We assume a spherical particle with the geometry parameterized with an outer radius R, a porosity ϵ_p, and a tortuosity $\tau = (\epsilon_p)^{-0.5}$. The governing equations are constructed according to porous electrode theory.

The species conservation equations are given by,

$$\varepsilon_p \frac{\partial c_l}{\partial t} = -\nabla \cdot \mathbf{F}_l - R_v, \tag{S2}$$

$$(1-\varepsilon_p)\frac{\partial c_s}{\partial t} = -\nabla \cdot \mathbf{F}_s + R_v. \tag{S3}$$

Where c_l is the salt concentration in the electrolyte, $\mathbf{F}_l$ is the flux of Li^+ ions in the electrolyte, $\mathbf{F}_s$ is the flux of neutral Li species, R_v is the volumetric rate of the reduction reaction, and c_s is the concentration of neutral Li species in the solid active material.

The volume averaged charge conservation equations in the particle are given by,

$$-\nabla \cdot \mathbf{i}_l = FR_v = \nabla \cdot \left(\sigma_l^{\text{eff}} \nabla \phi^l - \sigma_l^{\text{eff}} \frac{k_B T}{e} (1 - t_+) 2\Gamma_{\pm} \nabla \ln c_l \right), \tag{S4}$$

$$-\nabla \cdot \mathbf{i}_s = -FR_v = \nabla \cdot (\sigma_s^{\text{eff}} \nabla \phi^s). \tag{S5}$$

Here, $\mathbf{i}_l$ is the total ionic current density in the liquid, ϕ_s is the solid phase electronic potential, and ϕ^l is the electrolyte phase potential. ϕ^l is defined as a measurable quantity, as would be measured with a Li/Li$^+$ reference, which is related to the unmeasurable Galvani potential ϕ^{Galvani} by the electrochemical potential of Li ions: $F\nabla\phi^{\text{Li}} = F\nabla\phi^{\text{Galvani}} + \nabla\tilde{\mu}_{\text{Li}^+}$. The two conductivities, σ_l^{eff} and σ_s^{eff}, represent effective conductivities in the electrolyte and solid phases, given by $\sigma_l^{\text{eff}} = \frac{\varepsilon_p}{\tau}\sigma_l$ and $\sigma_{\text{s}}^{\text{eff}} = \frac{1-\varepsilon_p}{\tau}\sigma_{\text{s}}$, respectively. t_+ is the transference number of cations in the electrolyte.

The average thermodynamic factor $\Gamma_{\pm} = \frac{\Gamma_+ + \Gamma_-}{2}$ is defined based on the activity coefficients γ of the cations and anions, where $\Gamma_+ = 1 + \frac{\partial \ln \gamma_+}{\partial \ln c_l}$ (note that we are assuming a binary monovalent salt here).

Discretization

We discretize the porous particle via volume averaging and linearization. Consider N spherical shells along the radial coordinate r where we have $\{r_0, r_1\}, \cdots, \{r_{i-1}, r_i\}, \cdots, \{r_{N-1}, r_N\}$ for $i = 1 \cdots N$ over which the governing equations are integrated to obtain the shell balance equations.

Electrolyte

First, we discretize the electrolyte species balance equation (Eq. S2). Taking an effective diffusion coefficient of the salt $\mathcal{D}_{\text{l}}^{\text{eff}}$, $\mathbf{F}_{\text{l}}$ can be written as: $\mathbf{F}_l = -\mathcal{D}_l^{\text{eff}} \nabla c_l + \frac{t_+ \mathbf{i}_l}{F}$. By substituting this flux expression into Eq. S2 and defining concentration and reaction rate as the volume-averaged value in each shell, the equation for the quantities in the ith shell becomes:

$$\int_{V_i} \varepsilon_p \frac{\partial c_l}{\partial t} dV = -\int_{V_i} \nabla \cdot \left(-\mathcal{D}_l^{\text{eff}} \nabla c_l + \frac{t_+ \mathbf{i}_l}{F} \right) dV - \int_{V_i} R_v dV, \tag{S6}$$

$$\varepsilon_p V_i \frac{\partial c_l}{\partial t} = \mathcal{D}_l^{\text{eff}} \nabla c_l \Big|_{i+\frac{1}{2}} A_{i+\frac{1}{2}} - \mathcal{D}_l^{\text{eff}} \nabla c_l \Big|_{i-\frac{1}{2}} A_{i-\frac{1}{2}} - R_v V_i (1 - t_+). \tag{S7}$$

Here, V_i is the volume of the ith shell and $A_{i+\frac{1}{2}}$ is the face area (perpendicular to the radial direction) at the mid-point of the shell. We have utilized the divergence theorem to convert the volume integral. The ∇ operators could be further converted using mid-point approximations such as $\nabla c_l \big|_{i+\frac{1}{2}} = \frac{c_{l,i+1} - c_{l,i}}{\Delta r}$.

The electrolyte charge balance equation (Eq. S4) is analogously discretized to yield the charge

balance in each shell:

$$\begin{aligned}
&\sigma_l^{\text{eff}} \left(A_{i+\frac{1}{2}} \nabla \phi_{l,i+\frac{1}{2}} - A_{i-\frac{1}{2}} \nabla \phi_{l,i-\frac{1}{2}} \right) \\
&\quad - \sigma_l^{\text{eff}} \frac{k_{\text{B}} T}{e} \left(1 - t_+\right) 2\Gamma_{\pm} \left(\frac{A_{i+\frac{1}{2}} \nabla c_{l,i+\frac{1}{2}} - A_{i-\frac{1}{2}} \nabla c_{l,i-\frac{1}{2}}}{c_{l,i}} \right) \\
&= F R_v V_i.
\end{aligned} \tag{S8}$$

In the semi-dilute limit (no interference between positive and negative ions), the ambipolar chemical diffusivity of the salt is related to the ionic conductivity as:

$$\mathcal{D}_l^{\text{eff}} = \frac{RT}{F^2} t_+ t_- \frac{2\Gamma_{\pm}}{c_l} \sigma_l^{\text{eff}}. \tag{S9}$$

Substituting this relation into Eq. S8, we obtain:

$$\begin{aligned}
&\sigma_l^{\text{eff}} t_+ \left(A_{i+\frac{1}{2}} \frac{\phi_{l,i+1} - \phi_{l,i}}{\Delta r} - A_{i-\frac{1}{2}} \frac{\phi_{l,i} - \phi_{l,i-1}}{\Delta r} \right) \\
&\quad - F \mathcal{D}_l^{\text{eff}} \left(A_{i+\frac{1}{2}} \nabla c_{l,i+\frac{1}{2}} - A_{i-\frac{1}{2}} \nabla c_{l,i-\frac{1}{2}} \right) = t_+ F R_v V_i.
\end{aligned} \tag{S10}$$

The second term on the left-hand side of this equation can be substituted with Eq. S7:

$$\sigma_l^{\text{eff}} t_+ \left(A_{i+\frac{1}{2}} \frac{\phi_{l,i+1} - \phi_{l,i}}{\Delta r} - A_{i-\frac{1}{2}} \frac{\phi_{l,i} - \phi_{l,i-1}}{\Delta r} \right) - F \varepsilon_p V_i \frac{\partial c_l}{\partial t} = t_+ F R_v V_i. \tag{S11}$$

Since we intend to exclude salt diffusion effects, we can set $t_+ = 1$ so that no salt concentration gradients occur in the porous particle. Then, $\frac{\partial c_l}{\partial t}$ also becomes zero. With these conditions, Eq. S11 simplifies to

$$\sigma_l^{\text{eff}} \left(-A_{i+\frac{1}{2}} \frac{\phi_{l,i+1} - \phi_{l,i}}{\Delta r} + A_{i-\frac{1}{2}} \frac{\phi_{l,i} - \phi_{l,i-1}}{\Delta r} \right) = -F R_v V_i. \tag{S12}$$

Note that we have multiplied a minus sign on both sides. Then, Eq. S12 could be mapped to a circuit satisfying Kirchhoff's law:

$$I_{l,i+\frac{1}{2}} - I_{l,i-\frac{1}{2}} = I_{\text{ct},i} \tag{S13}$$

where $I_{l,i}$ is total ionic current in the ith shell in the radial direction.

$$I_{l,i\pm\frac{1}{2}} = -\sigma_l^{\text{eff}} A_{i\pm\frac{1}{2}} \frac{\Delta \phi_{l,i\pm\frac{1}{2}}}{\Delta r} \tag{S14}$$

$I_{\text{ct},i}$ is the total *oxidation* reaction current inside the ith shell.

$$I_{\text{ct},i} = -F R_v V_i = j_0 a_p V_i \tilde{\eta}_i. \tag{S15}$$

Here, for the second equality in Eq. S15, we have defined a_p as the electrochemically active area per volume. Also, we have linearized Butler-Volmer kinetics $j_{\text{ct}} = j_0 \left[-e^{-\alpha\tilde{\eta}} + e^{(1-\alpha)\tilde{\eta}}\right]$ (units in current density) to $j_{\text{ct}} = j_0\tilde{\eta}$, where $\tilde{\eta} = \frac{\phi_s - \phi_l - \phi_{s,\text{eq}}}{RT/F}$ is the dimensionless overvoltage for an oxidation reaction (*i.e.* positive voltage drives an oxidation current, which is $j_{\text{ct}} > 0$). To construct a circuit, it is more convenient to express the exchange current density in terms of an area-specific charge transfer resistance: $j_0 = \frac{RT/F}{\rho_{\text{ct}}}$, which leads to:

$$I_{\text{ct},i} = \frac{V_i}{\rho_{\text{ct}}} a_p \left(\phi_s - \phi_l - \phi_{s,\text{eq}}\right)_i . \tag{S16}$$

It is seen that the charge transfer resistance of shell i is:

$$R_{\text{ct},i} = \frac{\rho_{\text{ct}}}{a_p V_i} \quad [\Omega] \tag{S17}$$

Similarly, the ionic resistance of shell $i \pm \frac{1}{2}$ is:

$$R_{\text{ion},i\pm\frac{1}{2}} = \frac{\Delta r}{\sigma_l^{\text{eff}} A_{i\pm\frac{1}{2}}} \tag{S18}$$

Solid (Active Material)

Charge conservation of the solid phase (Eq. S5) can be discretized in an analogous manner by doing a volume integral over shell i and multiplying a minus sign on both sides, providing:

$$\sigma_s^{\text{eff}} \left(-A_{i+\frac{1}{2}} \frac{\phi_{s,i+1} - \phi_{s,i}}{\Delta r} + A_{i-\frac{1}{2}} \frac{\phi_{s,i} - \phi_{s,i-1}}{\Delta r}\right) = F R_v V_i . \tag{S19}$$

This equation also maps to Kirchhoff's current law:

$$I_{s,i+\frac{1}{2}} - I_{s,i-\frac{1}{2}} = -I_{\text{ct},i} . \tag{S20}$$

We see from a comparison between Eqs. S13 and S20 that ionic current is converted to electronic current due to the charge transfer current (that is, electronic current and ionic current are on opposite sides of a charge transfer resistor in a circuit representation). Here, the electronic currents are:

$$I_{s,i\pm\frac{1}{2}} = -\sigma_s^{\text{eff}} A_{i\pm\frac{1}{2}} \frac{\Delta\phi_{s,i\pm\frac{1}{2}}}{\Delta r} . \tag{S21}$$

The electronic resistance of the shells are:

$$R_{\text{elec},i\pm\frac{1}{2}} = \frac{\Delta r}{\sigma_s^{\text{eff}} A_{i\pm\frac{1}{2}}} . \tag{S22}$$

Next, we describe the neutral Li concentration in the active material c_s. We discretize Eq. S3 and describe it for a shell i with volume-averaged c_s:

$$(1-\varepsilon_p)\left.\frac{\partial c_s}{\partial t}\right|_i V_i = -\left(F_{s,i+\frac{1}{2}}A_{i+\frac{1}{2}} - F_{s,i-\frac{1}{2}}A_{i-\frac{1}{2}}\right) + R_v V_i. \tag{S23}$$

Now, recall that our intention is to allow for infinitely fast solid diffusion within each shell, but no solid diffusion between shells, so that we can exclude solid diffusion effects. This condition corresponds to $F_{s,i\pm\frac{1}{2}} = 0$, providing (after multiplying F):

$$F(1-\varepsilon_p)\left.\frac{\partial c_s}{\partial t}\right|_i V_i = FR_v V_i. \tag{S24}$$

The right-hand side corresponds to the total reduction reaction current in shell i, *i.e.* $-I_{\mathrm{ct},i}$. Meanwhile, the total chemical capacitance of shell i is:

$$C_{\mathrm{ch},i} = F(1-\varepsilon_p)V_i\left(-\frac{\partial c_s}{\partial \phi_{s,\mathrm{eq}}}\right). \tag{S25}$$

The minus sign indicates that Li concentration decreases with increasing Nernst voltage of the active material. Then Eq. S24 becomes:

$$C_{\mathrm{ch},i}\left.\frac{\partial \phi_{s,\mathrm{eq}}}{\partial t}\right|_i = I_{\mathrm{ct},i}. \tag{S26}$$

We see that chemical capacitance is charged as a result of oxidative charge-transfer current (*i.e.* a series connection between chemical capacitance and charge-transfer resistance in a circuit representation).

Time-domain simulations with the porous particle model

Using the electrolyte-penetrated porous particle model, we also simulate GITT measurements and examine the correlation between the time-domain extracted Warburg coefficients and R_{CT} from the simulated EIS behavior. The simulated time-domain data is analyzed using the same procedure as with the experimental data (Eq. 3 in the main text), yielding the apparent Warburg coefficient A_{w}. The results reproduce the experimental findings as well as the simulated EIS results, showing strong positive correlations in A_{w} vs. salt concentration (Supplementary Fig. 13a) and A_{w} vs. R_{CT} (Supplementary Fig. 13b).

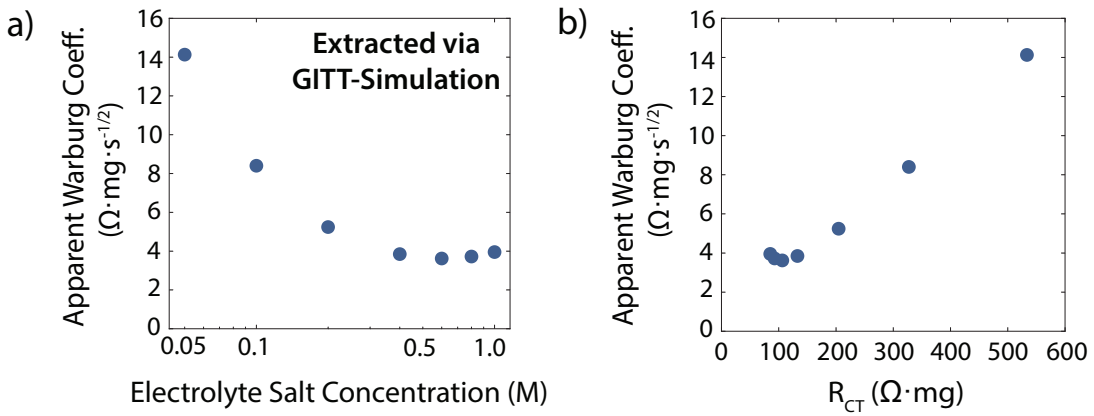

Supplementary Fig. 13: Porous particle model evaluated via time-domain simulations. **(a)** Extracted apparent Warburg coefficients from simulating the GITT protocol used in experiments. **(b)** Confirmation of the positive correlation between the GITT-simulated Apparent Warburg coefficients and R_{CT}.

Dependency on Particle Porosity Profiles

Here, we address the question on how particle porosity profiles affect low-frequency impedances.

First, consider uniform changes in porosity. Since the low-frequency impedance resembles the behavior of diffusion, an easy way to anticipate the impact of porosity is to consider how porosity would change the effective diffusivity in a diffusion-controlled system. As known from effective medium theory, the effective diffusivity of a medium scales with ε/τ (porosity divided by tortuosity). Then, the Warburg coefficient would scale with $\sqrt{\varepsilon/\tau}$ in such a system. In the porous particle case where the Warburg coefficient is controlled by the transmission-line effect from the electrolyte-penetrated pores, the apparent Warburg coefficient still behaves similarly as in a diffusion-controlled system; *i.e.* the apparent Warburg coefficient scales with $\sqrt{\varepsilon/\tau}$.

Next, consider the impact of non-uniform porosity. Here, it is useful to recognize which time scale controls the determination of the Warburg coefficient. In an EIS analysis where the scaling behavior of Z vs. $f^{-1/2}$ is relied on to extract a Warburg coefficient, it is typically the higher frequency part of the low-frequency region that controls the parameter determination. For example, if one observes a finite-length behavior but still relies on the Z vs. $f^{-1/2}$ scaling, that is equivalent to extracting the Warburg coefficient from the 45 degree region on a Nyquist plot. Such a region would occur at frequencies higher than the region where impedance starts to resemble that of a pure capacitor. Similarly in a time-domain analysis like GITT, it is the shorter time scales showing a $\sqrt{t}$ behavior that is typically used to extract a Warburg coefficient. Overall, we see that the shorter time scales (higher frequencies) of the diffusion-like behavior controls the determination of the Warburg coefficient in these techniques. Then, when the porosity is non-uniform inside a particle, it would naturally be the porosity near the surface that controls the extracted Warburg coefficient.

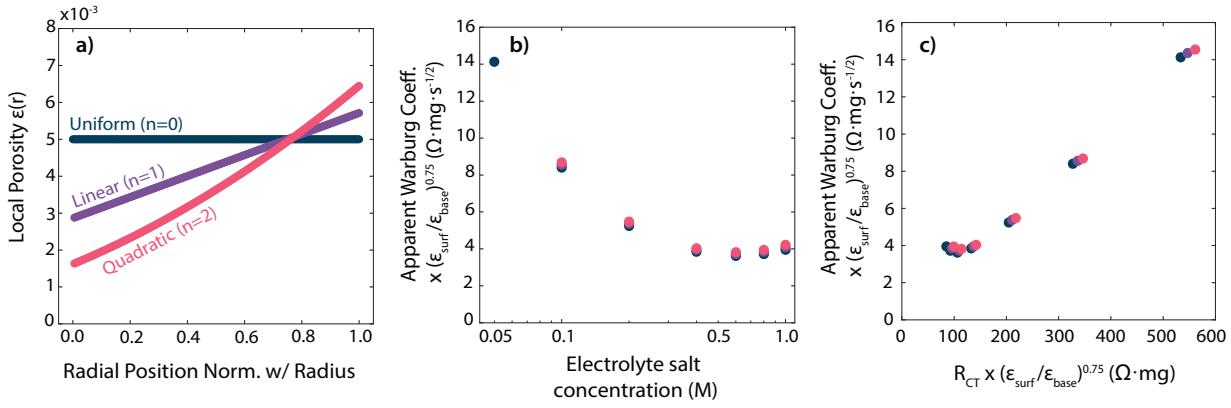

Supplementary Fig. 14: Scaling behavior of the Warburg coefficient in a particle with non-uniform porosity. a) Three different porosity profiles considered in the model. b) Apparent Warburg coefficients normalized with $\varepsilon^{0.75}$ of the surface showing similar dependencies on the salt concentration. Note that tortuosity is simultaneously scaling via $\tau = \varepsilon^{-0.5}$. c) The Warburg vs R_{CT} correlation, showing that the macroscopically determined R_{CT} also scales with $\varepsilon^{0.75}$. ε_{base} refers to the volume-weighted-average porosity, while ε_{surf} is the porosity at the outer surface of the particle.

We confirm this porosity-scaling argument with model simulations. We allow particle porosity to vary over the radial direction of the particle, as plotted in Supplementary Fig. 14a. Here, the volume-weighted-average porosity is kept identical between three cases. Next, apparent Warburg coefficients are extracted using GITT simulations (the uniform porosity case in Supplementary Fig. 14a is identical to that shown in Supplementary Fig. 13). By scaling the apparent Warburg coefficients with $\sqrt{\varepsilon/\tau} = \varepsilon^{0.75}$ (we are assuming $\tau = \varepsilon^{-0.5}$) using the porosity of the surface of the particle, it is seen the curves collapse upon each other, as shown in Supplementary Fig. 14b. R_{CT} also shows similar scaling behavior, seen in the correlation plot in Supplementary Fig. 14c.

Supplementary Note 7 EIS results from dense monolithic particles

We conducted EIS measurements on single crystalline $Li_xNi_{0.83}Mn_{0.05}Co_{0.12}O_2$ particles (dense monolithic particles) to see if the Warburg coefficient vs. R_{CT} correlation diminishes in non-porous particles. The morphology of the single crystalline particles is shown in the Extended Data Figure 1a of the main text.

For the experiment, electrodes were prepared in the same manner as those made using agglomerate particles, but with the addition of carrying out the electrode coating process in an Ar glovebox (due to the air-sensitivity of high-Ni content materials). Electrochemical conditioning and EIS measurements were conducted following the same procedure as agglomerate particle electrodes.

The results are summarized in Extended Data Figs. 1b-d, where it is seen that the biggest difference compared with porous agglomerate particles is a lack of correlation between the Warburg coefficient and R_{CT}. The correlation coefficient is 0.12 (Extended Data Fig.1d), whereas it was $0.85 - 0.88$ for porous agglomerate particles investigated in Fig. 3. This finding supports the idea that particle porosity makes a strong contribution to the Warburg coefficient via transmission line effects.

Meanwhile, we find that the Warburg coefficient is still not independent of the electrolyte salt concentration, as seen in Extended Data Figs.1b-c. This observation indicates that, as in the agglomerate particles, the Warburg coefficient is not solely controlled by the solid-state diffusion of Li in these dense particles. The implication is that we still have sources that contribute to the rate distribution for accessing chemical capacity, but particle porosity is no longer the dominant source of that. This finding supports the idea presented in Fig. 5b: that a Warburg-like behavior is not an exclusive indicator of diffusion.

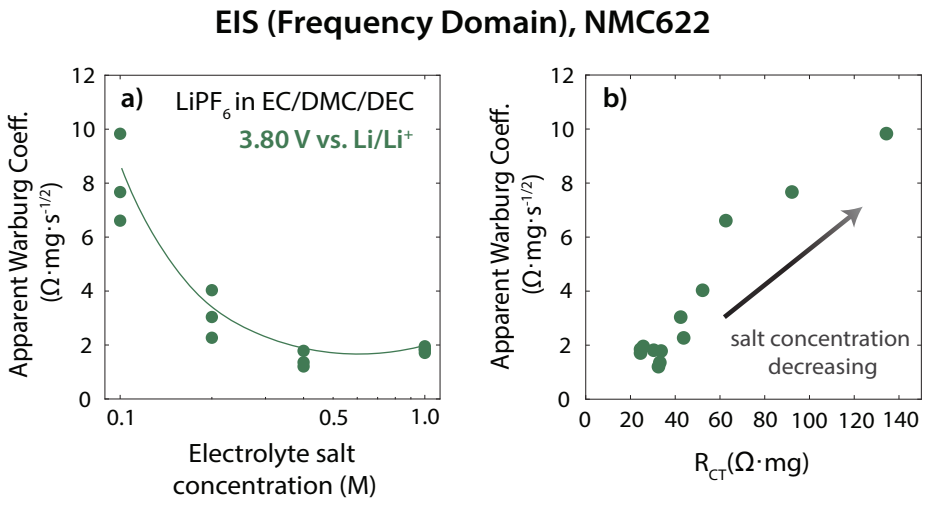

Supplementary Fig. 15: EIS investigation of thin electrodes made with $Li_xNi_{0.6}Mn_{0.2}Co_{0.2}O_2$ agglomerate particles. **(a)** Apparent Warburg coefficients extracted from EIS measurements vs. $LiPF_6$ salt concentration in the electrolyte. **(b)** A strong correlation between the apparent Warburg coefficients and R_{CT}, similar to the behavior found from NMC111 agglomerate particles. The material was obtained from Umicore. The solvent of the electrolyte had ethylene carbonate, dimethyl carbonate, and diethyl carbonate with a 1:2:1 ratio by volume. The formation cycles and EIS measurements were (inadvertently) conducted at 45 °C.

Supplementary Note 8 A_w-R_{CT} correlation from NMC622 agglomerate particles

To demonstrate that the strong correlation between A_w and R_{CT} is a general effect that could be expected from particle porosity, we test if a similar correlation is observed from a different active material. We obtain agglomerate particles of a different composition ($Li_xNi_{0.6}Mn_{0.2}Co_{0.2}O_2$; NMC622) produced by a different manufacturer (Umicore), and produce thin electrodes similar to the NCM111 electrodes (active material loading <0.6 mg cm^{-2}). The measured EIS results are summarized in Supplementary Fig. 15, where a similarly strong correlation between A_w and R_{CT} is observed from NMC622 agglomerate particles.

Supplementary References

S1. Osterrieth, J. W. M. *et al.* How Reproducible are Surface Areas Calculated from the BET Equation? *Advanced Materials* **34,** 2201502 (2022).

S2. Kuo, J. J., Kang, S. D. & Chueh, W. C. Contact Resistance of Carbon–Li_x(Ni,Mn,Co)O_2 Interfaces. *Advanced Energy Materials* **12,** 2201114 (2022).

S3. Kang, S. D. & Chueh, W. C. Galvanostatic Intermittent Titration Technique Reinvented: Part I. A Critical Review. *Journal of The Electrochemical Society* **168,** 120504 (2021).

S4. Kang, S. D. *et al.* Galvanostatic Intermittent Titration Technique Reinvented: Part II. Experiments. *Journal of The Electrochemical Society* **168,** 120503 (2021).